CHAPTER 3

Numerical simulation and experimental investigation for design of a carbon fiber tow pneumatic spreading system

Numerical simulation and experimental investigation for design of a carbon fiber tow pneumatic spreading system

Abstract

The work successfully designs a high efficient carbon fiber pneumatic spreading system. The internal flow field of the fiber pneumatic spreader was first simulated by solving Reynolds-averaged Naiver-Stokes equations, and the characteristics of the flow pattern in the spreader under various operation conditions were analyzed in terms of the mass flow rate and the velocity distributions. Meanwhile, the fluid visualization can be made before the spreading experiments. Comparisons of numerical results with measured velocity and pressure distributions were made to determine the accuracy of the employed method. A good agreement was found in both qualitative and quantitative analysis. A new variable, spreading evenness, was defined to specify the dispersing extent of fibers in a carbon fiber tow during the fiber pneumatic spreading process. By the spreading evenness, a quantitative comparison of a spread carbon fiber tow can be made and the optimum condition can be easily obtained at fiber spreading experiments. Photographic techniques were simultaneously applied to record the spreading procedures of carbons fibers. By the computational modeling and the spreading experiment, both the dispersing mechanism of carbon fibers and the interaction between the fibers and the airflow were understood. The evenness for a spread carbon fiber tow is influenced by air velocity at a given fiber-transporting rate, and the preliminary opening in the fiber tow is conducted by axial airflow. The performance of the fiber tow pneumatic spreader

system was better than prior studies, and the use of numerical analysis combined with

the fiber spreading experiment was useful for the development of the fiber pneumatic

spreading system.

. Introduction

In recent years, metal coated carbon fiber has been considered a promising material widely used as electrical contact devices, power semi-conductor devices, EMI (electromagnetic impulse) shielding, electrical brush and sink etc., owing to its high electrical conductivity, thermal conductivity, excellent wear resistance and high specific strength [1-6]. Above all, the importance of EMI shielding relates to the high demand of today's society on the reliability of electronics and the rapid growth of radio frequency radiation source. Therefore, metal-coated carbon fibers have great potential application as structural and functional materials in the future. The primary concern, however, relates to the difficulty of coating metal uniformly on continuous carbon fiber tows, and the chemical reaction at the interface between carbon fibers and metal.

A very thin and uniform coating over a fiber surface can promote the characteristics of carbon fiber composites; therefore, many methods have been proposed for the preparation of metallic deposition to improve and enhance the surface state of carbon fibers. However, the variation in the thickness of the coating on a carbon fiber tow has been observed. The variation between fibers on the inside of each bundle and those on the outside, however, is up to 20% ~ 90% [2, 4, 7-12]. The thickness of the layer on the monofilaments in the center of the fiber tow is considerably less than that of the layer deposited on the monofilaments at the outer of the tow. The results demonstrate that the EMI shielding capability of the fibers decreased as the coating thickness reduced, but the strength of the fibers decreased with increasing coating thickness [1, 4, 13-16]. Therefore, significant difference of the

mechanical behaviors and the physical properties yielded between the inner and outer fibers of a tow. The outer fibers in a tow are well activated during surface treatment, but the inner fibers in the tow are barely activated. The excess of compact carbon filaments is responsible for the non-uniform activation and the non-uniformity of the subsequent coating in a carbon fiber tow [11, 12]. It may not be possible to get an identical thin film and coat less than 0.2 μm thin layer on each fiber in a carbon fiber tow [2, 8, 17-18]. The change in the film thickness is as a function of the distance from the axis of the fiber tow and as the relative concentration of the chemicals as a function of the difference from the axis of the fiber tow for different positions in the reactor and for different deposition conditions. Deposition onto the central fibers is difficult; reactants are prevented from approaching the inner fibers. Thus, if the fibers are separated uniformly, it is advantageous for the improvement of fiber coatings [15, 19, 20].

Process and apparatus were developed for pneumatically spreading carbon filaments from a tow bundle to produce a sheet or a ribbon in which the filaments were separated and maintained in parallel [21-24]. The carbon fiber tow is comprised of thousands of filaments and the filaments are interacted with air in the pneumatic spreader. Baucom and Marchello were the first to attempt to design a pneumatic spreader [21]. They modeled a single fiber suspended in air under both a pressure drop and tow tension, and derived a formulation from orifice equation to predict the spread angle of a carbon fiber tow in the spreader. Comparisons of the experimental data for a 12k tow (containing 12,000 filaments) with the single fiber prediction indicated that the results were not satisfactory because there is a large deviation in the

spread degree between the experiment and the model. They concluded the flow-field is too complex in the spreader to know the interaction between the airflow and fibers, for the model derived from Bernoullis' ideal assumptions can not calculate and present the overall status of airflow. Also, the model of the single fiber prediction can not describe the internal flow-field of the spreader. Newell and Kawabe et al. focused their research on the design and processing factors of an effective pneumatic spreading system, respectively [22, 23]. They qualitatively examined the spreading characteristics of the carbon fiber tow in the spreader under various conditions; however, the discussion of the interaction between the flow fluid and the carbon fiber tow was unclear and incomplete because the flow field in the spreader remained unknown. Klettet al. employed a pressurized air-comb to separate the tow bundle before a coating process [24]. Also, they qualitatively illuminated the uniform spreading of a fiber tow exposed individual filaments by the air-comb for subsequent coating, but neither the procedures of tow spreading in the air-comb nor the spreading degree of the fiber tow were discussed. Accordingly, the spreading degree for a carbon fiber tow was considered in a very limited sense in the cited works, only a few which considered the evenness of a spread tow. When the fiber tow cannot be uniformly spread, some of the fibers pile up tightly. Without effective spreading, the effects of fiber bridging may become severe [23].

The critical part of the spreading process is the design of the fiber spreader itself. None of the cited investigations explored the effect of the airflow by the spreader design, and none of them qualitatively and quantitatively analyzed the internal flow patterns of the fiber spreader in detail. A highly chaotic or turbulent flow field would

bring about the variation in air velocity and airflow agitation in the spreader. Agitation can entangle fibers, making fiber spreading difficult and damaging the fibers. The characteristics of the internal flow field in the pneumatic spreader will be given by the design. This present work aims to establish a three-dimensional (3-D) model of the spreader by applying a computational fluid dynamics (CFD) method combined with far field treatment to study the internal flow field of the spreader. The CFD method was also implemented to visualize velocity fields, pressure and streamlines distribution, and thus elucidates the spreading mechanism of the new design spreader to optimize the design factors. The fiber pneumatic spreader is used to estimate experimentally the effect of air velocity on a carbon fiber tow. The goal is to develop an effective pneumatic fiber spreading system that can uniformly spread the fiber tow for post treatment, such as surface treatment or surface coating. The spreading process of a carbon fiber tow is recorded photographically. Moreover, a method of measurement is constructed to evaluate the distribution of the spread carbon fiber tow.

. Computational Techniques

The computational fluid dynamics methodology using the Reynolds-averaged Navier-Stokes (RANS) equations with no-slip boundary conditions was adopted to investigate the internal flow field of the pneumatic spreader. Finite difference approximations were employed to solve the transport equations with a body-fitted grid system. The incompressible and isothermal Reynolds-averaged Navier-Stokes equations are:

$$\frac{\partial u_j}{\partial x_j} = 0$$

$$\frac{\partial u_i}{\partial t} + \frac{\partial u_i u_j}{\partial x_i} + \frac{1}{\rho}\frac{\partial p}{\partial x_j} + \frac{\partial}{\partial x_j}\left(\overline{u_i' u_j'}\right)$$

$$-\frac{\partial}{\partial x_j}\left[v\left(\frac{\partial u_i}{\partial x_j} + \frac{\partial u_j}{\partial x_i}\right)\right] = 0 \quad , \quad i,j = 1,2,3$$

Where u_j is the velocity; p is the pressure; ρ is the constant density; v is the molecular kinematic viscosity; u_i', u_j' are the fluctuation parts of the velocity u_i and u_j, and $\overline{u_i' u_j'}$ is the Reynolds stress tensor, which can be modeled by the eddy viscosity hypothesis:

$$\overline{u_i' u_j'} = \tilde{\tau}_{ij} = \frac{1}{\rho}\hat{\tau}_{ij} = \frac{2}{3}\delta_{ij}k - \frac{2}{3}\mu_\tau \nabla \cdot u_i \delta_{ij} + \mu_\tau\left(\nabla u_i + \left(\nabla u_i\right)^T\right)$$

Here, k= $\frac{1}{2}\overline{u}^2$ is the turbulent kinetic energy, and μ_τ is the turbulent viscosity. This has to be prescribed by a turbulent model.

The turbulent model can be described by a generic k-ε model as [25]:

82

$$\rho \frac{\partial k}{\partial t} + \rho \nabla \cdot (u_i k) = \nabla \cdot ((v + \sigma_k v_T) \nabla k) + \tilde{\tau}_{ij} \nabla \cdot u_i - \rho \varepsilon$$

$$\rho \frac{\partial \varepsilon}{\partial t} + \nabla \cdot (u_i \varepsilon) = \nabla \cdot ((v + \sigma_\varepsilon v_T) \nabla \varepsilon) + c_1 \varepsilon / k \, \tilde{\tau}_{ij} \nabla \cdot u_i - c_2 \rho \frac{\varepsilon^2}{k}$$
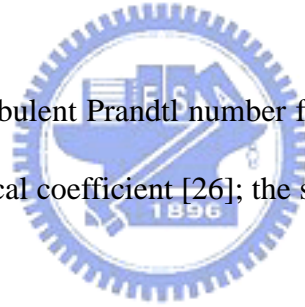
where $\sigma_k = \dfrac{k^2}{(c_2 - c_1)\sqrt{c_\mu}}$

k (Von Karman constant) = 0.4187

The eddy viscosity is calculated from:

$$v_T = c_\mu \rho \frac{k^2}{\varepsilon}$$

where σ_k and σ_ε are the turbulent Prandtl number for k and ε, respectively, and the

c_1, c_2 and c_μ are the empirical coefficient [26]; the set of model constants employed

is summarized in Table   .

. Boundary Conditions

As shown in Fig. 3-1(a), the geometry of the 3-D spreader model was defined first in a physical space (x, y, z). It was symmetrical in the vertical plane (x-y plane), so only half of the geometry was simulated to reduce the computer time. In most work of simulation, the boundary conditions at inlets were used to setting to be a uniform velocity that was quoted from measured data, or used ambient pressure for an internal flow field. In the present study, the inlet velocity was unknown, and making measurements in the case of sudden contraction was difficult. Therefore, the fluid flow is characterized in the far field. Thus, the computational domain was extended along the x-, y- and z-direction as depicted in Fig. 3-1(b).

The multiblock approach was used to maximize computational efficiency and save memory [27, 28]. The multiblock grid divided the solution domain into subdomains, and each subdomain has its associated subgrid or block. In multiblock grids, data are transferred from one block to another using a generalization of the periodic boundary conditions. The blocks were built on each side of the spreader model. Therefore, the boundary condition at the outer surface of each block could be specified by the atmospheric pressure (101300 Pa), and the flow field was computed from the external flow field to the internal flow field. The grid is structured and orthogonal curvilinear. The number of nodes and elements in the fluid domain were 137,800 and 129,600 respectively. Grid convergence was examined to ensure that the resolution of this mesh was adequate. Doubling the number of nodes changed the solution by less than 0.01%.

The boundary conditions were as follows.

(1) Symmetry plane:

$$V = W = 0$$

$$\frac{\partial U}{\partial x} = 0 \quad , \quad \frac{\partial \phi}{\partial x} = 0$$

where $\phi = k$, ε *and* p

(2) Pressure boundaries:

The computational domains were extended in the mathematical grid, to enable pressure boundaries to be created on the surfaces of the blocks, as shown in Fig. 3-1(b). For the surfaces were sufficiently far downstream, fixed values of all variables could be specified at the pressure boundaries.

p=101300 (Pa)   (atmospheric condition).

U=V=W=0   (free stream)

(3) Outlet

Static pressure was introduced at the outlet to model the outflow boundary. Various static pressures were used in the computation to elucidate the flow field in the 3-D spreader model. They were 101200 (pressure drop = 100 Pa), 101250 (pressure drop = 50 Pa) and 101270 Pa (pressure drop = 30 Pa) respectively. This approach was useful for predicting the experimental conditions, and comparing velocities computed from various pressure data and other measurements.

(4) Walls

The boundary wall was fixed and a no-slip condition was imposed on all velocity components. Many variables varied rapidly in the near wall regions of the flow and,

instead of using extremely fine grids in these regions, their behavior was specified with wall functions [25].

Discretization was carried out using the finite volume method. The governing equations were integrated over the control volume and reduced to algebraic equations, which followed conservation laws. In order to avoid pressure-velocity decoupling problems, arising from the fact that pressure and velocity were calculated in the same location, the convection flux through each cell face was calculated using the modification proposed by Rhie and Chow [29], extended here for a multi-block grid. The SIMPLE algorithm was used as a pressure-correction method [30], to derive the pressure equation from the continuity equation. In this work, since the transient evolution was not of interest, the time step was optimized for fast convergence; acceleration techniques like false time step were applied [26]. Therefore, a typical simulation of the 3-D model on the base mesh required 300 MB of memory, and consumed a total CPU time of 7.237×10^4 second. The program was executed on a vector computer, the CRAYJ916 super computer, with eight 100MHz processors and 1GB of main system RAM.

. Experimental

4.1 Experimental Setup

Experiments were conducted using the setup schematically presented in Fig. 3-2. The main elements were comprised in sequence of: the tow feed spool, the tension control device, the pneumatic tow spreader, the vacuum pump and the take-up spool. The fibers from the carbon fiber tow that contained 12000 filaments were passed through a fiber guide into a first friction roller. The first roller was synchronized with the second friction roller at a constant speed. Both two rollers were controlled by a variable speed driver. Hence, the fibers between these two rollers, which were subsequently spread in the pneumatic spreader, remained under low tension that was maintained by the tension control device. For the airflow rate in the pneumatic spreader, the vacuum pump sucked air, and gave a stable control of flow rate that was measured by a multiple tube flow meter and a precision pressure controller. After the fibers spread and left the second roller, the fibers were taken up by a take-up system.

The pneumatic spreader was formed by PAN (polyacrylonitrile) pieces, which were transparent, allowing the spreading procedure of carbon fibers to be photographed. It was fixed by two steel plates to prevent vibration during spreading the fibers. The fiber entrance, inlet-2, had a half-width of 2.5mm. The fiber exit, inlet-1, had a final fiber spread half-width of 25mm. The clapboard contained nine slots are parallel to the symmetry plane, as shown in Fig. 3-1. Each slot is 5mm wide and 10mm apart; the first slot is behind the inlet-1 50mm long.

According to the simulation results, the pneumatic spreader would be modified, and spreading experiments would be undertaken to test the applicability of the 3-D

mathematical model. First, the downstream pressures and velocities near the outlet were measured by precision pressure controller and digital micro-manometer, under various flow rates without carbon fiber tow, and the velocities would be compared with the calculated data to confirm the accuracy. Spreading experiments of a fiber tow were executed at various fiber transporting rates and air flow rates. Photography techniques were used to record the processes of fibers separated. The photographs were taken from the top view. Five Nikon FM2 cameras were used and each was fitted with a 52mm lens. The single-frame photographs were taken with shutter speeds of 1/15 to 1/60 seconds, so that the images showed how fibers was spread and moved in the pneumatic spreader.

4.2 Image Process

This study more effectively determines the spreading degree of a carbon fiber tow than other investigations, but the evenness for a spread fiber tow is more important than the spreading degree. If the fiber tow were not uniformly separated, some of the fibers would be tightly piled up. Therefore, the spreading evenness for a carbon fiber tow in the spreading process should be considered first. A carbon fiber tow was spread in 50 mm wide. The LECO 2001 Image Processing System was used to evaluate the evenness of the spread fiber tow. Firstly, the image (50 mm × 50 mm, width × length) of the spread fiber tow was captured by using a CCD, and an image was taken at intervals of 50 mm. The, area fractions of five consecutive images of the fiber tow at a specified area (50×50 mm^2) were calculated using the image processing system at a setting gray level. The spreading evenness was determined by

the average value of the five area fractions.

Spreading evenness $= \Sigma \, Xi \, / \, 5$,

where $Xi(\%)$ is the area fraction of the spread fibers, $i = 1 - 5$.

Ⅴ. Results and Discussion

5.1 Analysis of the simulated flow pattern in the pneumatic spreader

Figure 3-3 illustrates the streamlines, which were plotted at the central plane (y = 2.5mm) of the pneumatic spreader. There were three of circulation (2, 3, and 4) and one low-pressure zone (1) in the spreader. The simulation yielded the following results:

(a) The air was sucked into and entered the spreader, and it was accelerated due to sudden contraction at inlet-1 and inlet-2. Accordingly, the circulation zone was formed by fluid viscosity and drag.

(b) The airflow entered inlet-1, and passed through the nine slots on the clapboard; therefore, two circulation zones were presented behind the clapboard.

(c) Additionally, a narrow low-pressure zone formed near the clapboard because the airflow passed through the separation location S; hence airflow separation generated. Air could not enter this zone near the clapboard, so it was thin and did not flow; thus, the pressure dropped. However, the area of the low-pressure zone declined as the air flux decreased.

In this moment, the main interest was the flow field between the symmetry plane and the clapboard owing to the fiber tow was spread in this region.

It was shown that the varieties of flow velocity appeared at inlet-1, inlet-2 and slots from the color level, since the cross-sectional area decreased. The velocity of airflow differed only a little between inlet-1 and inlet-2. That Q = ρVA is well known, where Q is the flux or mass flow rate; ρ is the fluid density; V is the fluid velocity, and A is the cross-sectional area of the inlet. The flux at inlet-1 was ten times greater

than that at inleat-2, and the slots on the clapboard were close to inlet-1. The airflow varied mainly near inlet-1, so this investigation on the discussion concentrated in the region between inlet-1 and the slots.

Figure 3-4(a) demonstrates a complete view of the W-velocity (lateral velocity) contour, which reveals a high lateral velocity at the slots. A close-up view of the W-velocity contour in the vicinity of the slots was shown in Fig. 3-4(b). The distribution of the lateral velocity W was reducing with the distance Z approaching symmetry plane; similarly, the more air flowed into the inner location, the more velocity W increased. Above all, the much variation in the velocity W existed behind the slots. Compared axial velocity U with the lateral velocity W in the fiber spread region, the U-velocity is much lager than W-velocity. To test the accuracy of the numerical simulation, the physical model was constructed according to the numerical parameters, and a series of experimental measurements were made, the downstream pressures and velocities near the outlet were measured by a precision pressure controller and digital micromanometer, under various flow rates without carbon fiber tow, and the velocities were compared with the calculated data as revealed in the Fig. 3-5. The computational data were in good agreement with the measured data. Similar trends were observed at the static pressure, 101,250 (pressure drop 50 Pa) and 101,200 Pa (pressure drop = 100 Pa).

The air flux was related to the fluid velocity and pressure in the spreader, and it was controlled by the flowmeter. Figure 3-6 indicates these measured values. The mean mass flow rate increased linearly with the axial velocity and was proportional to the mean static pressure. Similarly, the computational results exhibit the same trends

as the measured results. The converged solution was calculated from upstream to downstream; moreover, the upstream computational results had the same order in numerical error as the downstream. The simulated and measured data were both qualitatively and quantitatively similar; further, the 3-D computational results can be helpful for designing a pneumatic spreader. Although considering no fiber addition might not be precise enough to lead to an understanding of the interaction of fiber and air flow, the results gave us insight and led to the realization of the 3-D flow field. Therefore, the flow field can qualitatively understand before the fiber spreading experiment executed.

5.2 Effect of the air velocity

Figure 3-7 demonstrates spreading experiments of a carbon fiber tow. The fiber tow was hardly to be spread by air drag owing to the small air velocity, under the condition $V_F = 7$ m/min and $Q < 60$ L/min, where V_F is the fiber transporting velocity and Q is the flux. Therefore, it kept the original size about 5 mm. Figure 3-8 shows the results of the spreading experiment combined with the simulated flow field represented by streamlines. Carbon fiber tow was spread over a width of approximately 20 mm at the fiber exit under the constant fiber transporting velocity ($V_F = 7$ m/min), but flux Q was increased to 70 L/min, as revealed in Fig. 3-8 (left). As mentioned above, when air was sucked into the spreader, the main variations in the air velocity occurred near inlet-1 because of a sudden contraction in the cross-sectional area and an acceleration of airflow. Furthermore, the inlet-1 was more than ten times the flux of the inlet-2, as the area of inlet-2 was reduced during the

fiber tow passed. Hence, the fiber tow was fluffed and separated at fiber exit (i.e. inlet-1) by airflow. Subsequently, carbon fibers progressively moved to lateral side until 20mm wide, while the fiber tension was balanced with the drag force. From Fig. 3-3, it was readily comprehensive that the uniform flow existed in the range between the inlet-1 and slot-1 and the main flow velocity was axial velocity (U-velocity). The airflow was accelerated to a maximum axial velocity at the fiber exit. Transverse flow was produced downstream, for the airflow turned toward the clapboard. Hence, the lateral velocity W increased with decreasing the axial velocity, approaching the maximum near the inner slots. The axial velocity was 3.21 m/s and the lateral velocity near inner slots was 0.7 m/s, as shown in Fig. 3-8 (right).

While flux Q was increased to 90 L/min, it was seen that the fiber tow was easily spread, and most fibers shifted toward the clapboard and concentrated at the clapboard. As demonstrated in Fig. 3-9, the carbon fiber tow was spread over a width of 50 mm. During the spreading process, the separated fibers were gradually extended to the clapboard by the large axial velocity of approximately 5 m/s. However, the distribution of the lateral velocity increased abruptly near the clapboard, since the airflow turned toward the slots. Thus, as air flowed into the inner location, axial velocity decreased sharply. The lateral velocity W rose to 1.5 m/s at the inner slots, as indicated in Fig. 3-4. The air cross-flow provided a drag force to the carbon fibers. Finally, the fibers were dragged toward the clapboards, and the same width was maintained as the fiber exit. Similar spreading results were obtained under other conditions, with the same spreading procedures. The continuous fiber spreading procedures are summarized as the following three main steps.

(1) The fiber tow was initially spread out and fluffed at the fiber exit by the axial airflow.

(2) Fibers gradually moved toward lateral side, and the lateral velocity would influence the fiber movement.

(3) As the fibers moved closer to the clapboard, the transverse velocity increased; hence, the fibers were dragged toward the clapboard.

The proposed spreading procedures were more detailed and differed significantly from the procedures proposed by previous investigators. Baucom and Kawabe et al. argued that applying transverse air flow to carbon fibers results in tow spread across the pneumatic spreader. They neglected the preliminary opening in the fiber tow was conducted by axial airflow. Figure 3-10 illustrates the width of the unspread and spread fiber tow under different test conditions. To study the spreading evenness of the carbon fiber tow by the pneumatic spreading system, the area fraction of the fiber tow in areas of 50×50 (mm^2) was calculated by the above-mentioned method and the evenness of the spread fiber tow was thus obtained. The spreading evenness in Fig. 3-7, 3-8 and 3-9 was 10 (%), 36.3 (%) and 38.2 (%), respectively. The difference of the evenness can be realized by previous discussion.

5.3 Effect of the fiber transporting velocity

The spreading evenness increased with the air flux at a given fiber transporting velocity, but it decreased as the air flux increased beyond 80 L/min, because the lateral velocity was large as revealed in Fig. 3-10. Favorable spreading evenness was obtained under a certain condition, and similar trends were observed at other fiber

transporting velocities. The fiber transporting velocity caused a difference between values of the spreading evenness at small air fluxes, such as $Q = 70$ L/min. As the transporting velocity increased, the spreading evenness was improved at a constant mass flow rate. However, the spread fiber tow at $V_F = 7$ m/min and $Q = 80$ L/min yielded the evenness of 62.3(%). This is because the fibers separated were conducted by axial velocity; in addition, there was a short interaction time between airflow and fibers with high fiber transporting velocity. Therefore, the transverse-flow applied to the carbon fibers was limited; the values of the evenness differed a little at $Q = 90$ L/min for the three fiber transporting velocities. The higher lateral velocity droved carbon fibers rapidly toward the clapboard; consequently, more fibers were dragged toward the clapboard, reducing the evenness.

A carbon fiber tow will be hardly spread out during the spreading experiment, even though the air flux was raised to 90 L/min, if the fiber tow was static or at a low fiber transporting velocity $V_F < 1.5$ m/min. Thus, the fiber transporting velocity provided the frequency of fiber movement reducing the friction among each fiber, which made fibers easily separated. Moreover, it also supplied a relative velocity with respect to the airflow. In other words, the preliminary opening in a carbon fiber tow was conducted by the total axial velocity U_T. $U_T = U - (-V_F)$, where U is the axial velocity; V_F is the fiber transporting velocity, and minus sign expresses the opposite direction to the axial velocity. When the lateral velocity was small at $Q = 70$ L/min, the fibers were spread out by the axial velocity. The higher fiber transporting velocity ($V_F = 7$ m/min) results in a good spreading evenness. At this case, the U_T was 3.34 m/s at $V_F = 7$ m/min. The fiber transporting velocity would influence the fiber

separation as the air velocity smaller enough. However, the effect of the transporting velocity could be neglected at high air velocity, but no investigator has considered this effect. Newell and Kawabe employed a very large air flux of 720 L/min and the higher air velocity of 50 m/s, respectively, in the fiber spreading process. Notably, the spreading evenness can be used easily to compare quantitatively the spread fiber tows under various test conditions.

5.4 Effect of modifying the number of slots

The fiber spreading efficiency was obviously promoted, but the spreading evenness was still unsatisfied. The lateral velocity was an important parameter at the spreading experiments, as discussed above, and the evenness was almost constrained by air drag, which results from lateral airflow. The coverage of the lateral velocity was broad in the pneumatic spreader with nine slots. When the air flux was increased, the lateral velocity was distributed from the first slot to the ninth slot. The lateral velocity was higher at the inner location; therefore, the drag force would be sufficiently large to apply to the carbon fibers. Meanwhile, increase the air flux, and the axial velocity is also promoted. Hence, the spreading evenness cannot be improved further because the axial and lateral velocities are large. It was well known that the flux is constrained by the cross-sectional area, and fluid velocity is inversely proportioned to the cross-sectional area. Form the half of the geometry, as shown in Fig. 3-1(a), the cross-sectional area are 250 mm^2 at inlet-1 and 25 mm^2 at inlet-2, respectively. The total cross-sectional area on the clapboards is 450 mm^2 at the spreader with nine slots open. However, if the slots were reduced, the cross-sectional area on the clapboard

was smaller than that at inlets. Similarly, the airflow would be accelerated at inlet-1 and a given slot; above all, the lateral velocity could be increased and concentrated in front of the slot. The total axial velocity U_T can be controlled by adjusting the axial velocity combined with the fiber transporting velocity. Therefore, eight slots were sealed in the spreader, leaving only the first one opened.

Fig.3-11 shows the simulated flow pattern, it was observed that the air was sucked into the spreader and the airflow quickly passed through the first slot to the outlet as the air flux increased. The lower velocity was existed at fiber exit because the flux was constrained by the slot 1. Also, it was found that the flow pattern was significantly different from the spreader with nine slots open at the same boundary condition (as Fig. 3-3). The variation in the velocity was not obvious at inlet-1 nearby, but the coverage of lateral velocity was more concentrated between the symmetry plane and the clapboard. The air velocity at inlet-2 was much lower than that at the spreader with nine slots open under the same condition, as illustrated in Fig. 3-11(a). Disturbance and agitation can be avoided at a low air velocity. While the pressure drop was increased at the boundary condition, the physical phenomena were more significant as presented in Fig. 3-11(b).

Compared with the above experiment at inlet-1 nearby under the same conditions, it is shown in Fig.3-12 that the U-velocity component increased with increasing the pressure drop, and the increasing rate was larger at the spreader with nine slots open than that with one slot open. Simultaneously, the axial velocity at the spreader with one slot open was smaller than that with nine slots open under the same pressure drop of 50 Pa, even though the pressure drop increased to 70 Pa; however, the U-velocity

was still smaller than that at nine slots open. The results are attributed to the limited flux in the one slot. By the results, it was known that the air velocity will be easily controlled at fiber spreading experiment. Furthermore, when we examined the distribution of the axial velocity U from symmetry plane to the clapboard in front of slots, and compared one slot open with nine slots open under the same condition, as revealed in Fig. 3-13(a). Each curve represented the velocity variation of each slot from symmetry plane. The results present that U-velocity component decreased as the air flowed into the inner location at the spreader with nine slots open. The main reason was the airflow turned direction and the fluid friction as shown in previous paragraphs. There was a negative U-velocity around slot 9; this was because air flow came from inlet-2. The fluid velocity at one slot open was much lower than that at nine slots open. But it abruptly increased with the distance approaching clapboard from 0.65 m/s to 1.1 m/s. The U-velocity abruptly increased owing to a sudden contraction and an acceleration of airflow at one slot open.

For the cross-sectional areas were reduced to 50 mm^2 on the clapboards in the spreader with one slot open, the flux would be constrained by slot-1. Initially, the fluid was also accelerated at inet-1 as the airflow entered the spreader; however, the fluid was accelerated once again at slot-1 due to the sudden contraction. The lateral velocity W exhibited a significant difference between one slot open and nine slots open, as demonstrated in Fig. 3-13(b). The distribution of the W-velocity component was increasing with the distance approaching the clapboard at slots1, 5 and 9 with nine slots open because the air flow turn toward. The more air flowed into the inner position, the more velocity W increased. However, a large increase in lateral velocity

W was found at one slot open, and the distribution of the velocity W was larger than that at nine slots open.

The fibers spread experiments under the condition $V_F = 6$ m/min and $Q = 110$ L/min are demonstrated in Fig. 3-12. Initially, the carbon fiber tow moved in the spreader. Gradually, the fibers was spread out and fluffy at the fiber exit as presented in Fig. 3-14(a), because there was a maximum axial U-velocity at the exit (inlet-1) due to a sudden contraction and an acceleration of air flow. Sequentially, more fibers were spread out, and we could see the preliminary opening from the spread width at the inner location was smaller than that at fiber exit as shown in Fig. 3-14(b). Finally, fibers were dragged toward the clapboard and kept the width of the spreader, since the airflow turned toward the slot, as shown in Fig. 3-14(c). There were similar spread results at the other conditions, and the fiber spread procedure was all the same. In the experiment, the fiber tow was transported into the spreader at the lower fiber transporting velocity and fibers were separated and moved lateral side by a given total axial velocity U_T. Subsequently, the fibers were dragged to lateral side by the transverse flow. Consequently, we found that the fibers were spread out smoothly; additionally, the spreading evenness was improved and satisfied.

Hence, the high-speed transverse flow provided higher air drag to the carbon fiber tow. In the fiber spreading experiment, the fiber tow was transported into the spreader at a high fiber transporting velocity and fibers were separated and moved lateral side by a given total axial velocity U_T. Subsequently, the fibers were dragged to lateral side by the transverse flow. Consequently, the evenness in a carbon fiber tow was increased, and the fibers spread out smoothly. The calculated evenness reached 83 (%) at $V_F = 5$ m/min and $Q = 105$ L/min, as shown in Fig. 3-15(a). While the flux Q

was increased to 125 L/min, the fibers were dragged to clapboard, owing to the increase in the lateral velocity W. It can be seen that the partial spread fiber extend to the inner of the spreader about the location of the ninth slot, as illustrated in Fig. 3-15(b). Modifying the number of slots increased the spreading evenness; the flow field of the pneumatic spreader varied significantly and the velocity and pressure distributions differed from those of the spreader with nine slots.

To identify the non-uniform coating in a carbon fiber tow can be overcome by the pneumatic spreading process; two groups of spread and unspread carbon fiber tow coated with nickel by physical vapor deposition (PVD) and electroless plating were compared. The results showed that a uniform Ni coating could be obtained on each fiber in the spread carbon fiber tow, and the thickness of the Ni film could be coated on carbon fiber tow less than 0.2 µm. Similar results were also obtained in aluminum coated carbon fibers by PVD [31].
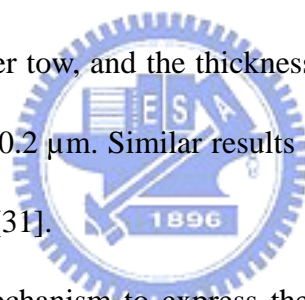
Therefore, we proposed a mechanism to express the procedures during a fiber tow separation. The mechanism was illustrated in Fig. 3-16. From previous discussion, we knew that the preliminary opening in a carbon fiber tow is started at fiber exit, i.e. inlet-1, and the uniform flow is located between slot-1 and inlet-1. There is a fiber transporting velocity V_F at fiber moved direction; on the contrary, there is a U-velocity at air flow direction, as depicted in the Fig. 3-16(a). Therefore, $U_T = U - (-V_F)$. We focused on the fibers at outside of a fiber tow, which were marked number 1, 2, 3 and 4. The $U_T > U_{in}$, where U_{in} is axial velocity in a fiber tow and $U_{in} \cong 0$, and $P_{in} > P_{out}$. Hence, fiber 1 was dragged out by the dragging force caused by the pressure difference at step 1 as shown in Fig. 3-16(b). Subsequently, fiber 2 and fiber

3 are also dragged out at step2, and finally the fiber 4 is dragged out. These

procedures are developed in a carbon fiber tow, and make fibers separation by the

preliminary opening.

. Conclusion

The internal flow field of the pneumatic spreader was first simulated by numerical investigation, and the work successfully developed a new and efficient fiber pneumatic spreading system. The spreading process of a carbon fiber tow was first visualized by the photographic technique. The performance is better than that at previous studies. The main results and of this investigation are summarized as follows:

1. By the three-dimensional mathematical model of the fiber pneumatic spreader, the simulated flow patterns are helpful to analyze the variation of airflow and to understand the internal flow-field of the spreader at different conditions.

2. The spreading evenness is first used and discussed in spread carbon fiber tow, and it is more useful than spreading degree in elucidating the spreading process of the fiber tow. The newly defined variable, spreading evenness, facilitates a quantitative comparison among the spread fiber tow under various test conditions, and the optimum conditions for the spreading process can thus be obtained.

3. The pneumatic spreading system outperforms systems described elsewhere, and a carbon fiber tow can be uniformly and efficiently spread out. The optimum conditions for fiber spreading are $V_F = 7$ m/min and $Q = 80$ L/min, for the nine slot pneumatic spreader, with a evenness of spread of 62.3(%).

4. The spreading evenness of a carbon fiber tow was constrained by the large air velocity; therefore, when eight slots in the spreader were sealed, the evenness of the fiber tow reached 83 (%), differing considerably from that in the flow field of the spreader with nine slots.

5. The fiber spreading procedures are proposed in detail by computational fluid modeling and experiment, and they can help in understanding the spreading process and the design of a pneumatic spreader.

. References

[1] Hung CY , Pai JF. Optimum conditions of electroless nickel plating on carbon

fibres for EMI shielding effectiveness of ENCF/ABS composites. Eur. Polym. J. 1998;

34(2): 261-7.

[2] Shi Z, Wang X, Ding Z. The study of electroless deposition of nickel on graphite

fibers. Applied Surface Science 1999; 140: 106-10.

[3] Wan YZ, Wang YL, Luo HL, Dong XH, Cheng GX. Effects of fiber volume

fraction, hot pressing parameters and alloying elements on tensile strength of carbon

fiber reinforced copper matrix composite prepared by continuous tree-step

electrodeposition. Materials Science & Engineering A 2000; A288: 26-33.

[4] Tzeng SS, Chang FY. Electrical resistivity of electroless nickel coated carbon

fibers. Thin Solid Films 2001; 388: 143-9.

[5] Chung DDL. Electromagnetic interference shielding effectiveness of carbon

materials. Carbon 2001; 39: 279-85.

[6] Dang Z, Shen Y, Fan L, Cai N, Nan C, Zhao S. Dielectric properties of carbon

fiber filled low-density polyethylene. Journal of Applied Physics 2003; 93: 5543-5.

[7] Abraham S, Pai BC, Satyanarayana KG, Vaidyan VK. Studies on nickel coated

carbon fibres and their composites. Journal of Materials Science 1990; 25: 2839-45.

[8] Abraham S, Pai BC, Satyanaryana KG. Copper coating on carbon fibres andtheir

composites with aluminium matrix. Journal of Materials Science 1992; 27: 3479-86.

[9] Yu JK, Li HL, Shang BL. A functionally gradient coating on carbon fibre for C/Al composites. Journal of Materials Science 1994; 29: 2641-7.

[10] Emig G., Popovska N, Schoch G., Stumm T. The coating of continuous carbon fiber bundles with SIC by chemical vapor deposition: A Mathematical model for the CVD-process. Carbon 1998; 36(4): 407-415.

[11] Clark, D, Wadsworth NJ, Watt W. Handbook of Composites 1, Strong Fibers, Elsevier Science Publisher B.V. 1985; 579-80.

[12] Thostenson ET, Li WZ, Wang DZ, Ren ZF. Carbon nanotube/carbon fiber hybrid multiscale composites. T. W. Chou, Journal of Applied Physics 2002; 91(9): 6034-7.

[13] Subramanian RV, Nyberg EA. Zirconia and organotitanate film formation on graphite fiber reinforcement for metal matrix composites. J. Mater. Res. 1992; 7(3): 677-688.

[14] Leonhardt G., Kieselstein E, Podlesak H, Than E, Hofman A. Interface problems in aluminum metal matrix composites reinforced with coated carbon fibers. Materials Science and Engineering 1991; A135: 157-160.

[15] Ranjan TPD, Pillai RM, Pai BC. Review- reinforcement coatings and interfaces in aluminum metal matrix composites. Journal of Material Science 1998; 33: 3491-3503.

[16] Lu G, Li X, Jing H. Electrical and shielding properties of ABS resin filled with nickel-coated carbon fibers. Composite Science and Technology 1996; 56: 193-200.

[17] Langdry CC, Barron AR. MOCVD of alumina-silica oxidation resistant coatings on carbon fibers. Carbon 1995; 33(4): 381-7.

[18] Ochiai S, Murakami Y. Tensile strength of composites with brittle reaction zones at interfaces. Journal of Materials Science 1979; 14(4): 831-840.

[19] Yang H, Gu M, Jiang W, Zhang G. Interface microstructure and reaction in Gr/Al metal matrix composites. Journal of Materials Science 1996; 31: 1903-7.

[20] Wang YQ, Zhou BL, Wang ZM. Oxidation protection of carbon fibers by coatings. Carbon 1995; 33(4): 427-33.

[21] Robert M. Baucom, Johseph M. Marchello. LaRC powder prepreg system. Sampe Quarterly 1990; 35: 175-188.

[22] Newell JA, Puzianowski AA. Development of a pneumatic spreading system for Kevlar-based SIC-precursor carbon fibre tows. High Perform Polym. 1999; 11: 197-203.

[23] Kawabe K, Tomoda S, Matsuo T. A pneumatic process for spreading reinforcing fiber tow. 42nd International SAMPE Symposium 1997; 65-76.

[24] Klett JW, Edie. DD. Flexible towpreg for the fabrication of high thermal conductivity carbon/carbon composites. Carbon 1995; 33(10): 1485-1503.

[25] Launder EB, Spalding BD. Mathematical Models of Turbulence. Academic Press, Londen 1972.

[26] Harwell Laboratory. CFX-F3D Version 1 User Manual, Oxfordshire, U.K., 1995.

[27] Tompson JF. Numerical Grid Generation. Elsevier, New York, NY, 1992.

[28] Tompson JF. Thames, FC, Martin CW. Auutomatic Numerical Generation of Body-Fitted Currvlinear Coordinate System for Field Containing Any Number of Arbitrary 2-D Bodies. J. Computational Physics. 1974; 15: 299-319.

[29] Rhie MC, Chow LW. Numerical study of the turbulent flow past an airfoil with trailing edge separation. AIAA Journal. 1983; 21(11): 1525-32.

[30] Patankar SV, Spalding DB, A Calculation Procedure for Heat, Mass and Momentum Transfer in Three-dimensional Parabolic Flows. Int. J. Heat Mass Transfer. 1972; 15: 1787-1808.

[31] Chen JC, Tsai KC, Chao CG. Development of a Novel Process for Metal Coated on a Carbon Fiber Tow by PVD and Electroless Deposition. Annual Symposium of Taiwan Association for Coating and Thin Film Technology. 2004, as press.

Table   . Model Constants Employed in the Computation

c_1	c_2	c_μ	σ_k	σ_ε
1.44	1.92	0.09	1	2.9076

SLOTS

INLET-1

25

50

195

OUTLET

110

1 2 3 4 5 6 7 8 9

CLAPBOARD

250

195

500

Origin

SYMMETRY
PLANE

O

INLET-2

2.5

125

Y(V)

Z(W)   X(U)

Unit: mm

(a)

SLOT-1

Extended Grids and
Pressure Boundary

Extended Grids and
Pressure Boundary

O

Origin

y(V)

z(W)   x(U)

(b)
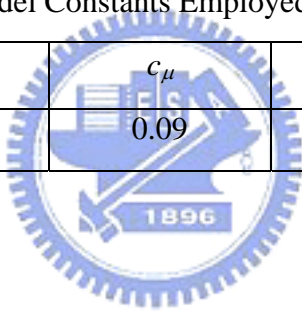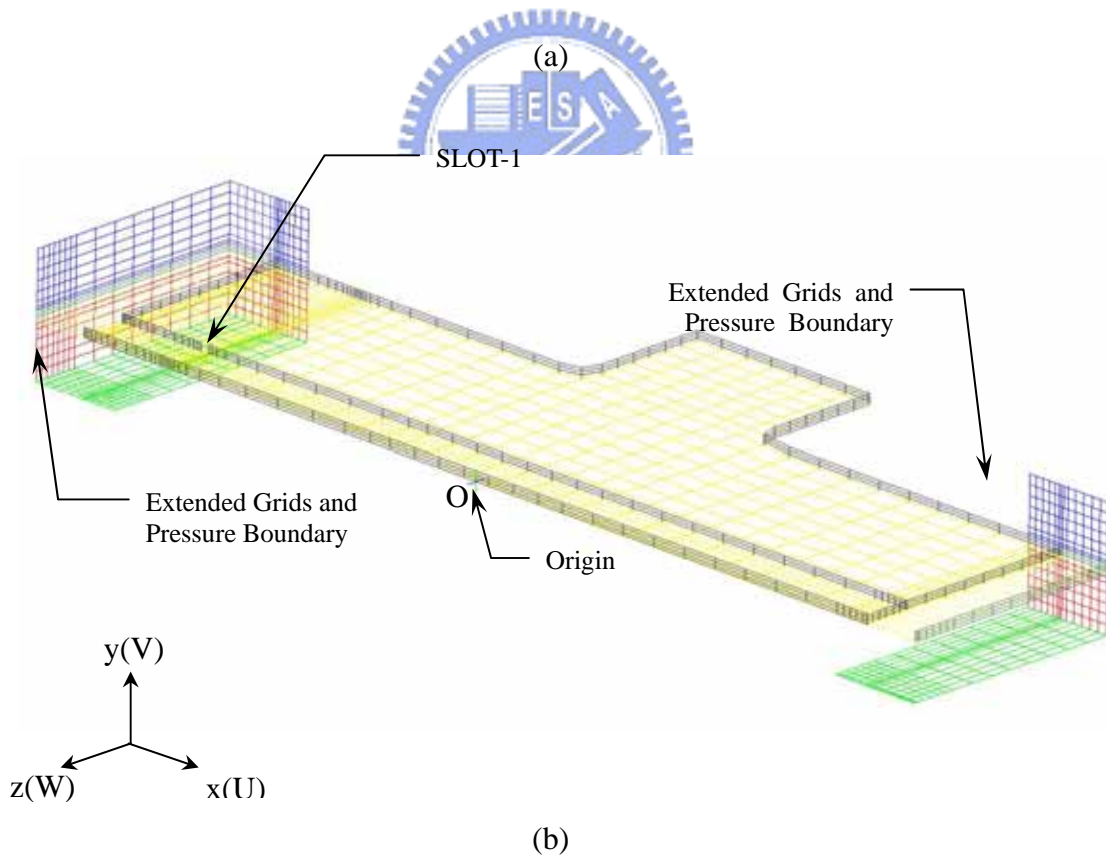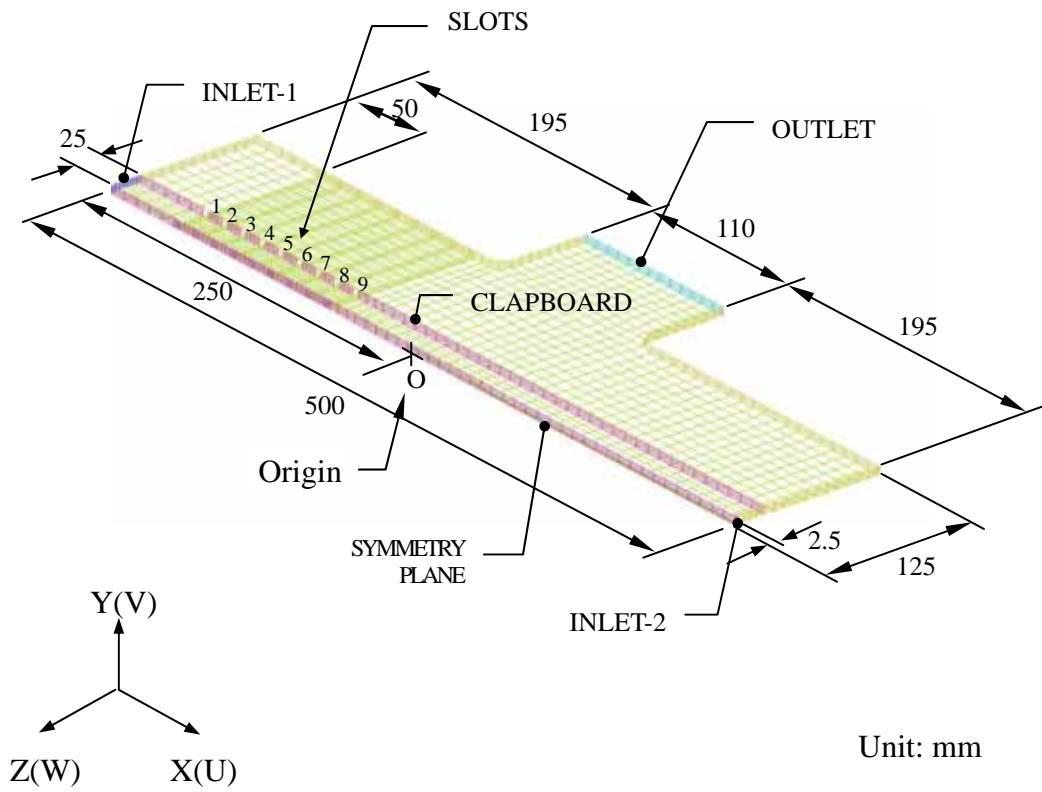
Fig. 3-1 (a) A three-dimensional mathematical model of
the pneumatic spreader, (b) A perspective of a far-field
treatment by multi-block technique (U, V and W are the
velocity compoments).
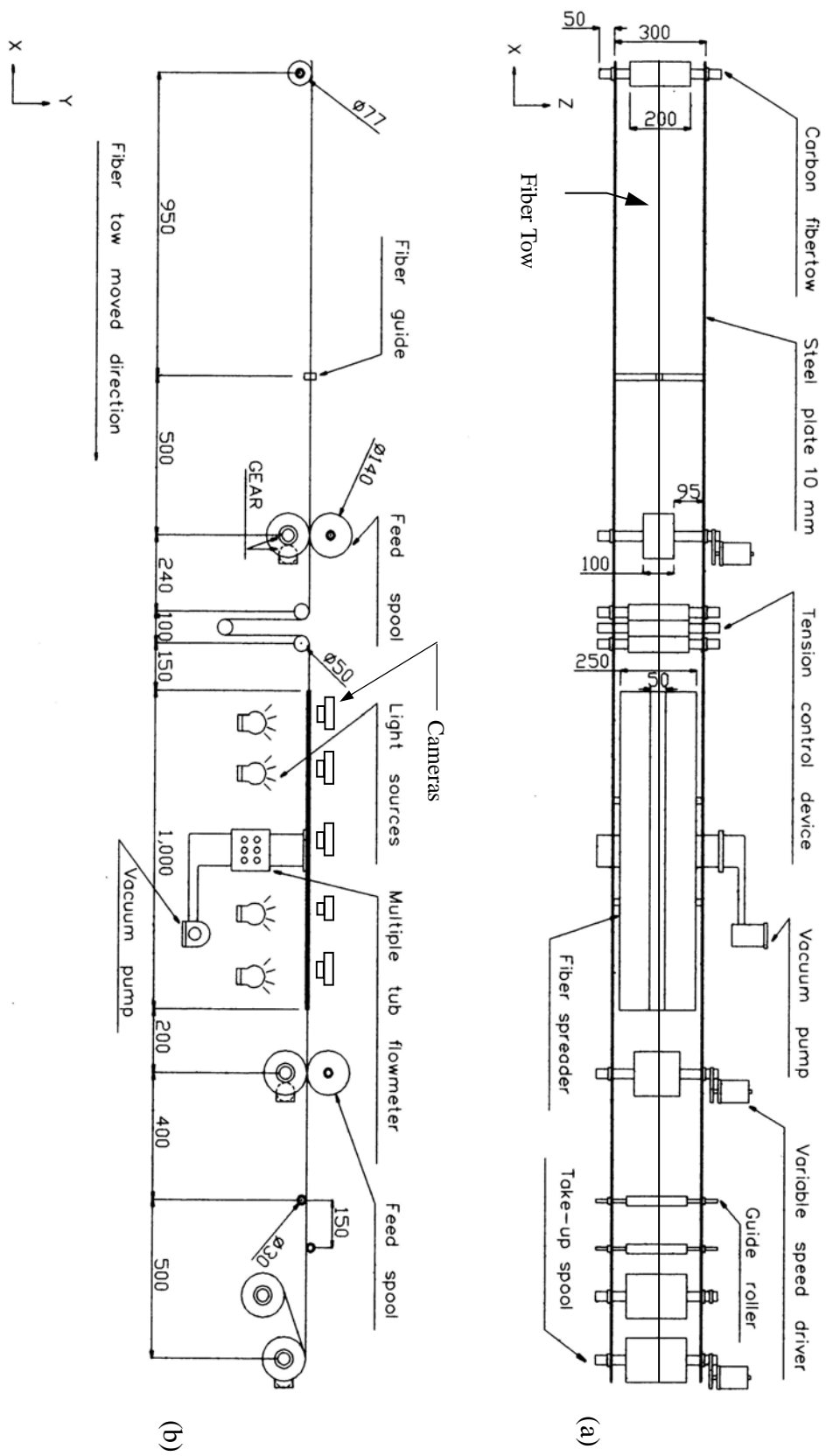
Fig. 3-2 Schematic of the experimental setup for spreading a carbon fiber tow (a) a top view, (b) a side view.
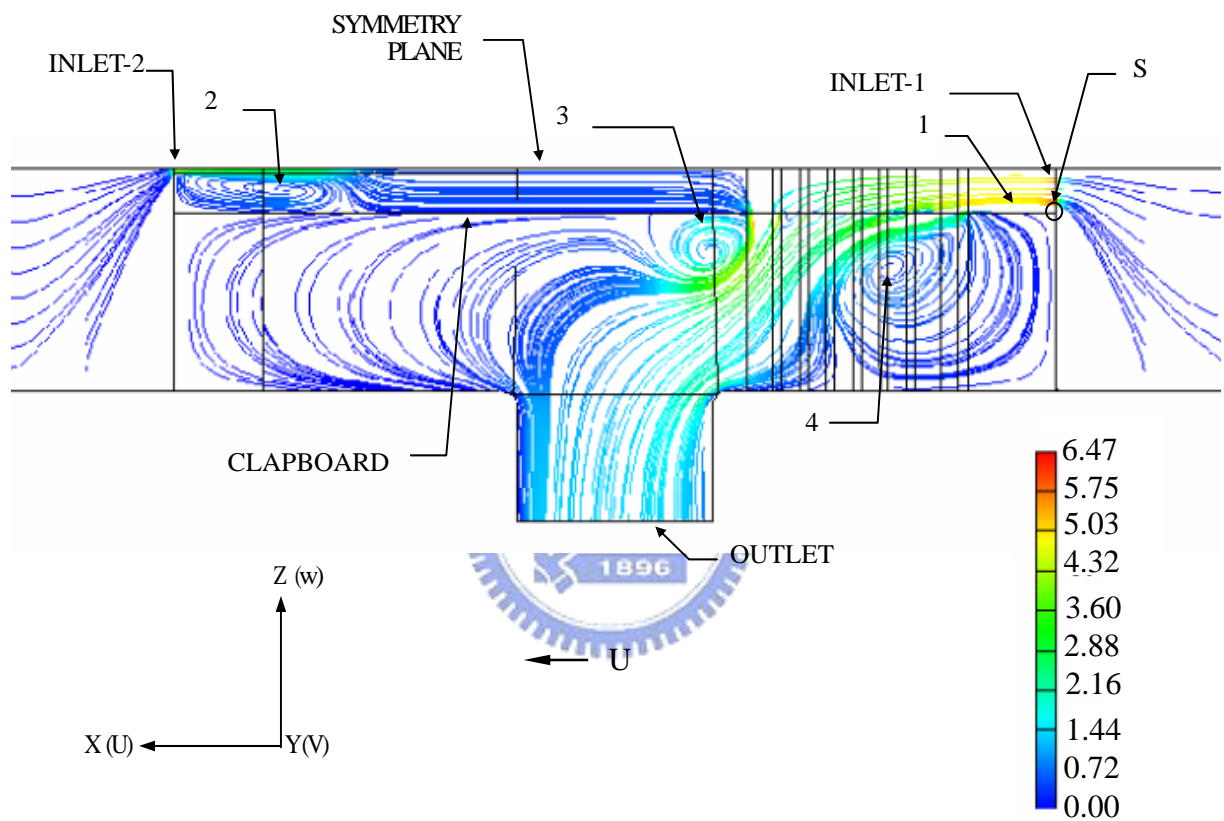
Fig. 3-3 A complete view of streamlines at the central plane (y=2.5 mm) under the pressure drop 50 Pa for the 9 slots designed pneumatic spreader.
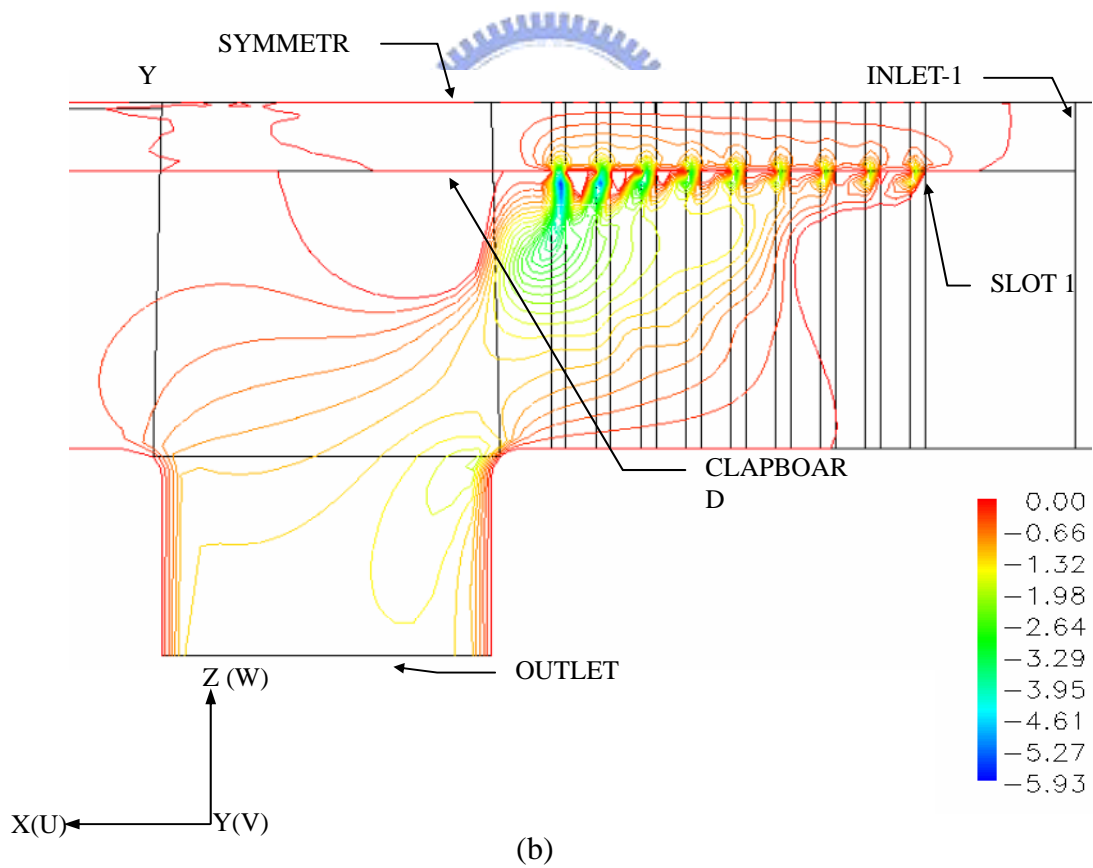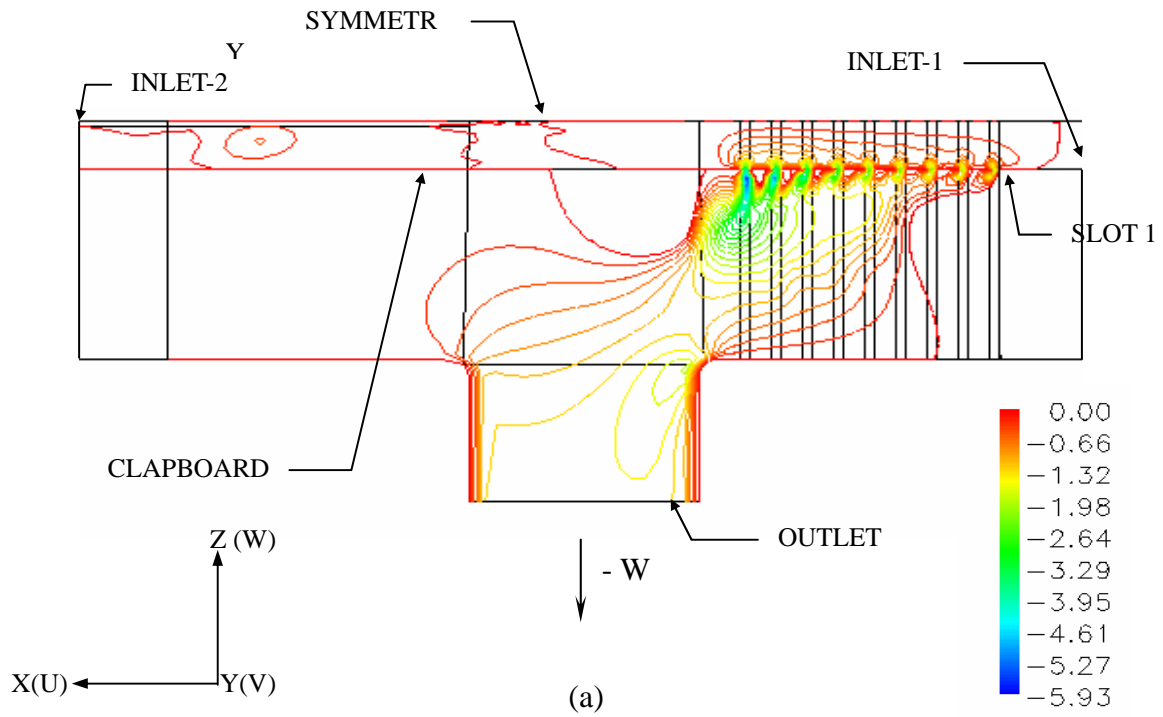
Fig. 3-4 W-velocity (lateral velocity) contour under the pressure drop 50 Pa: (a) a complete view and (b) a close-up view.
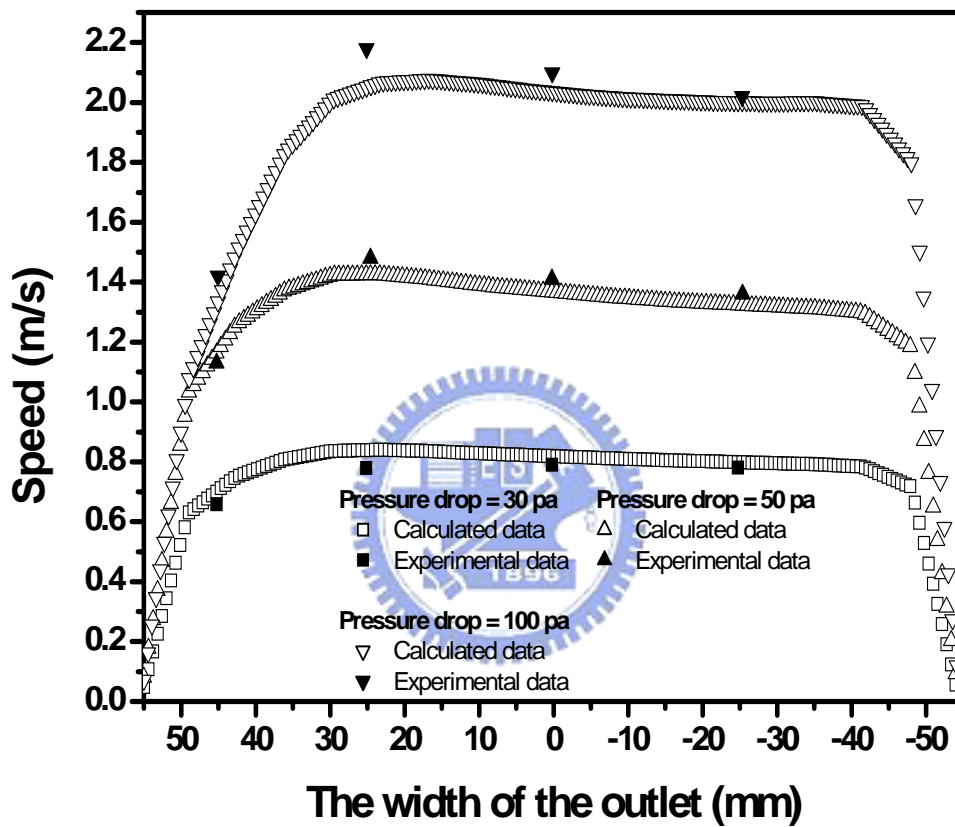
Fig. 3-5 Comparison of computational and measured speed at outlet under different conditions.
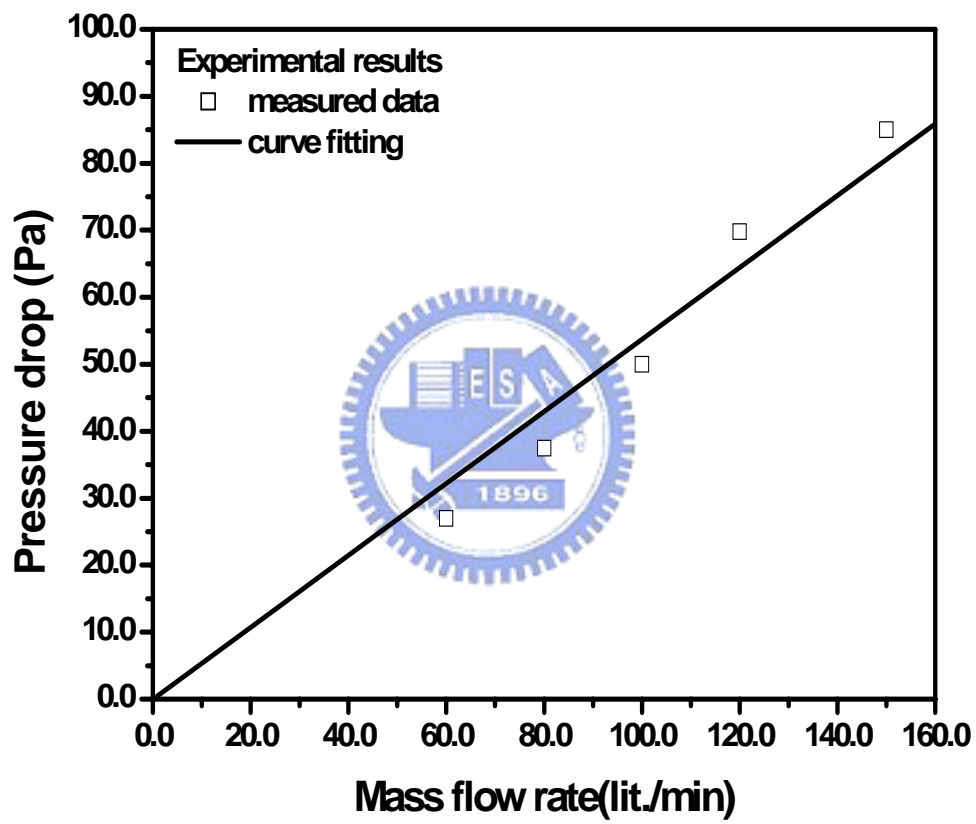
Fig. 3-6 The relations of the experimentally measured
mean mass flow rate Q and pressure drops at outlet
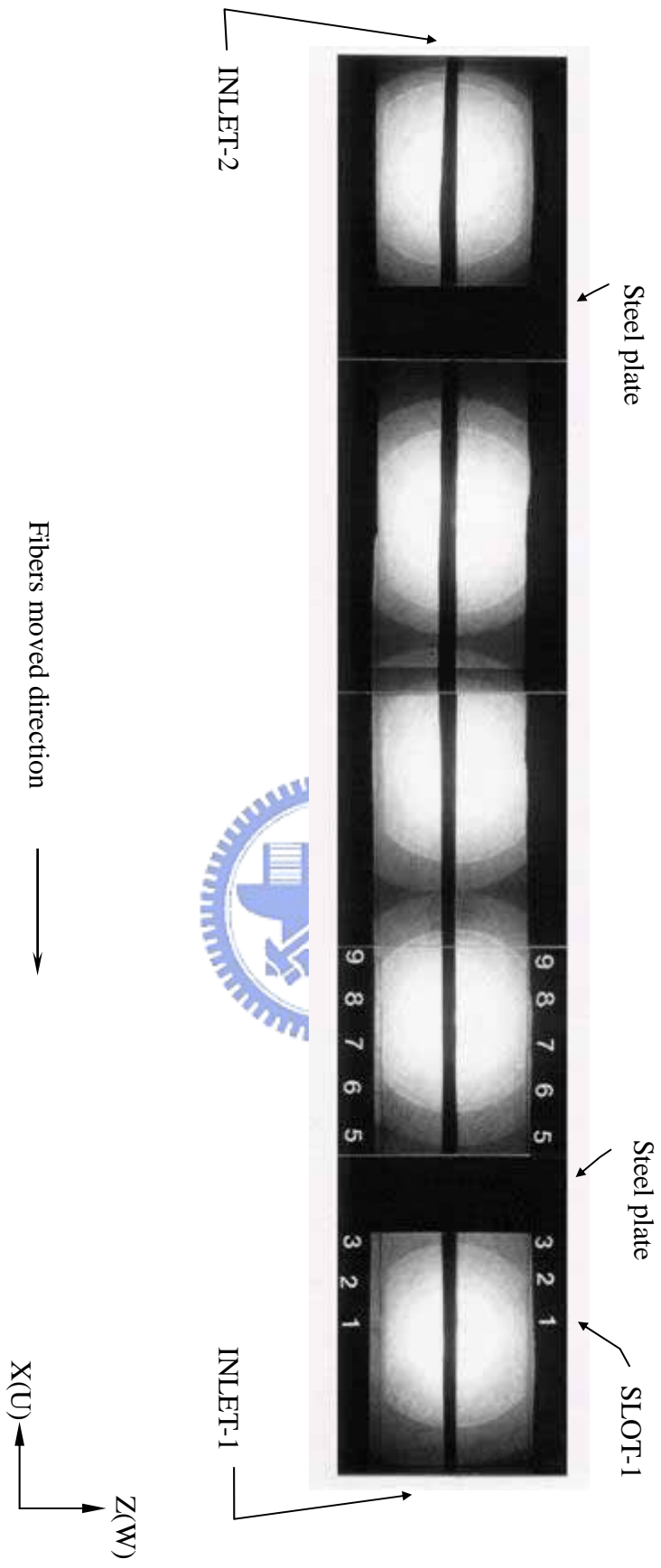
Fig. 3-7. Photograph of the spreading experiment on a fiber tow under $V_F = 7$ m/min and $Q < 60$ L/min.

115
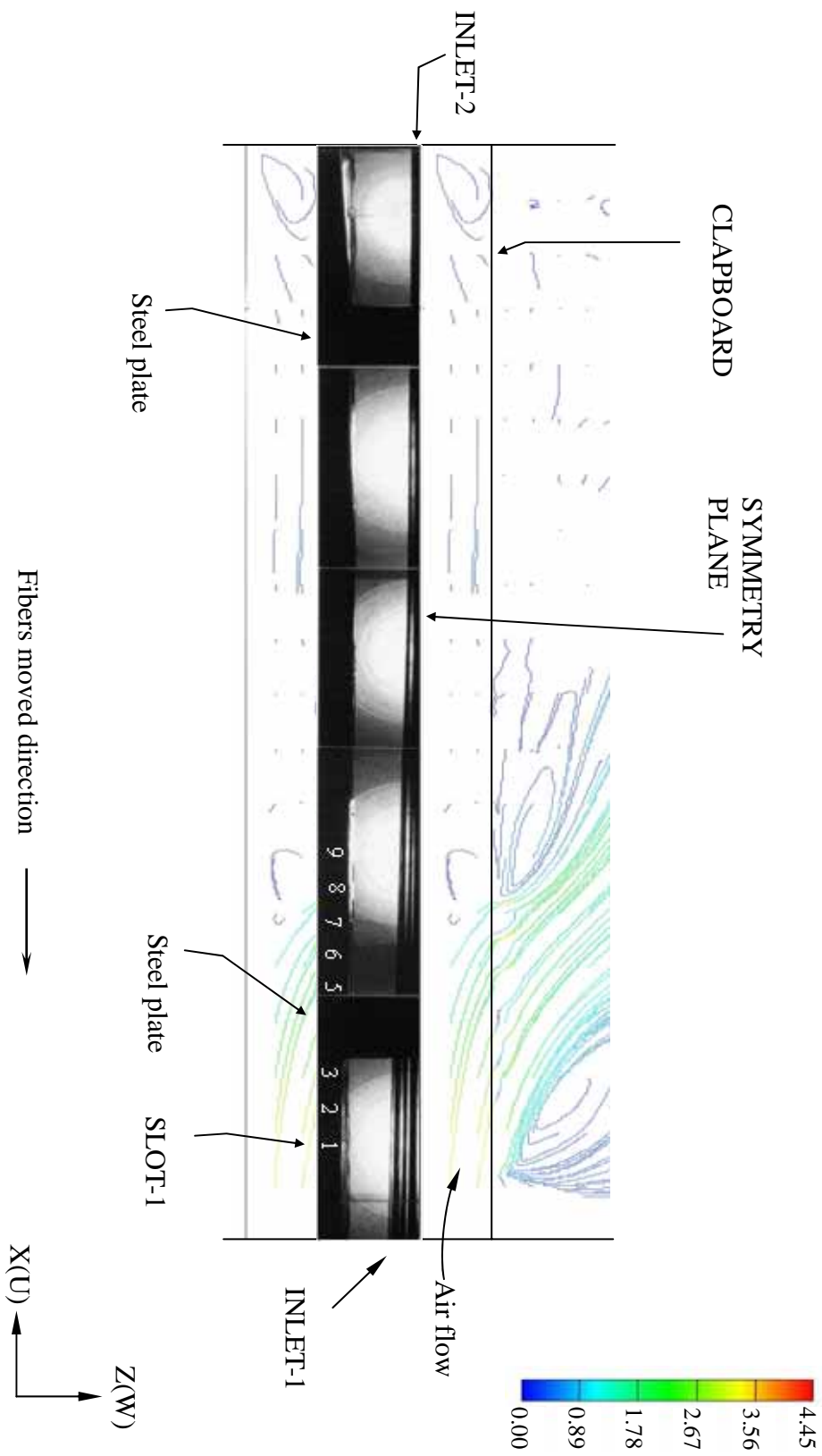
Fig. 3-8 . Photograph of the spreading experiment on a carbon fiber tow combined with the streamlines of the flow field under V_F = 7 m/min and Q = 70 L/min.
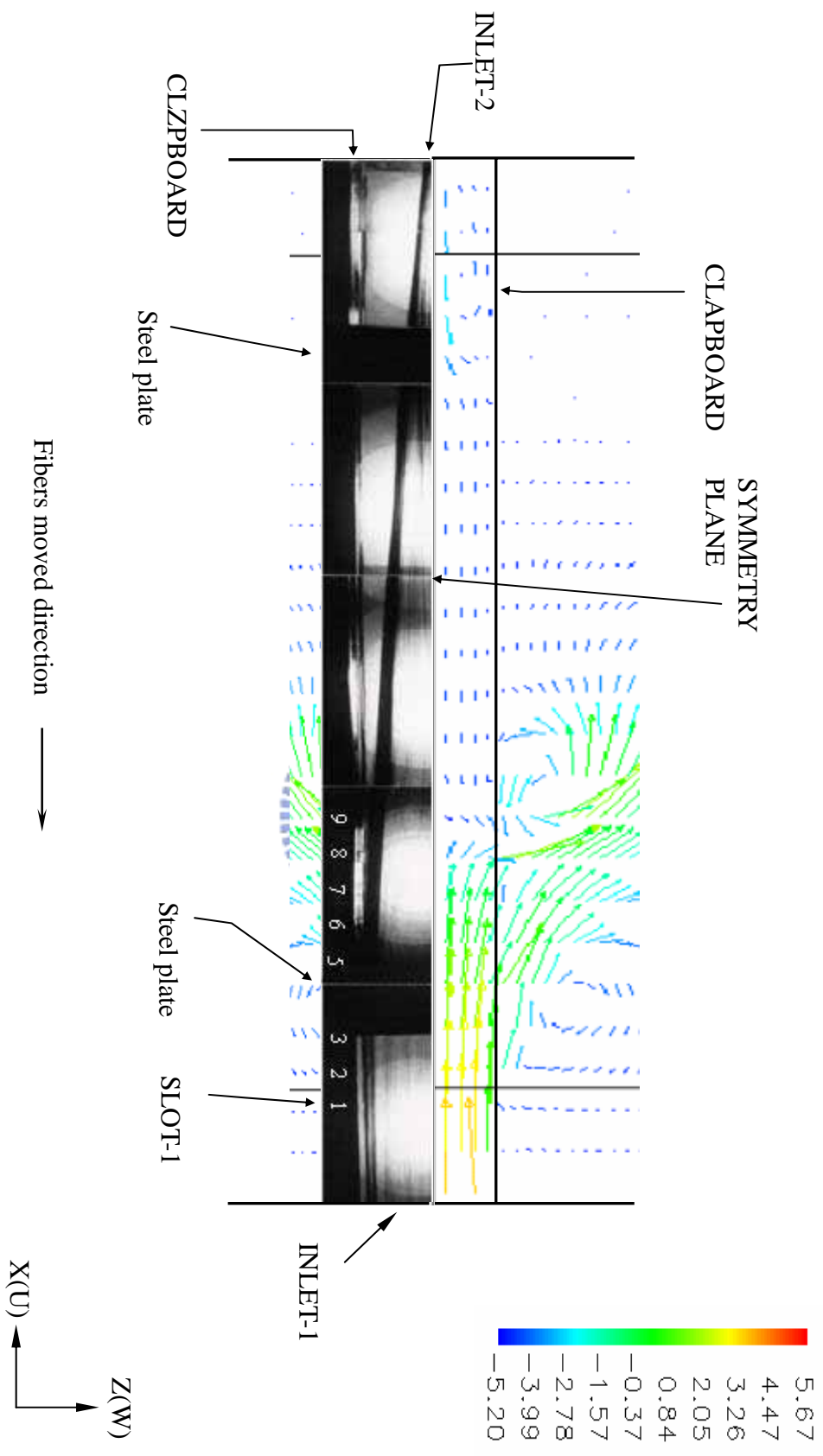
Fig. 3-9. Photograph of the spreading experiment on a fiber for combined with the velocity-vector representation of the flow field under $V_F = 7$ m/min and $Q = 90$ L/min.

117
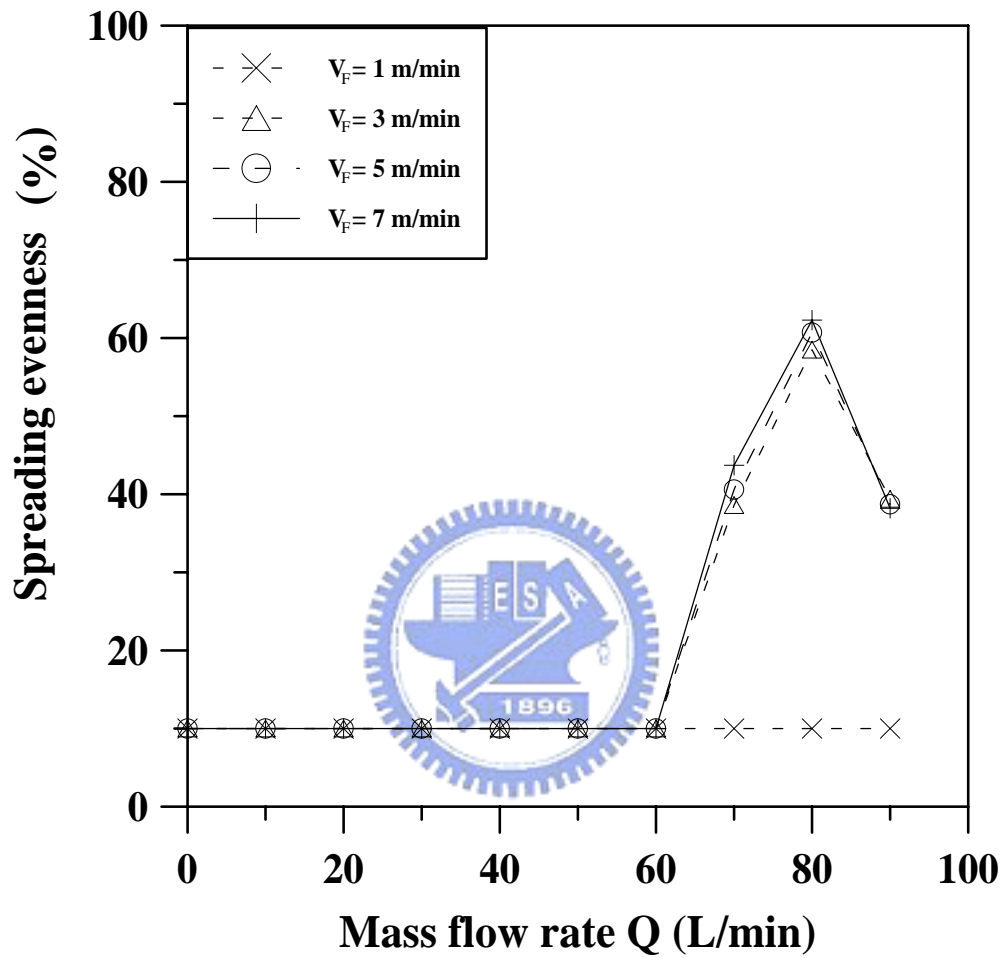
Fig. 3-10 The relations of the fiber spreading evenness and the mass flow rates under different fiber-transporting velocities.
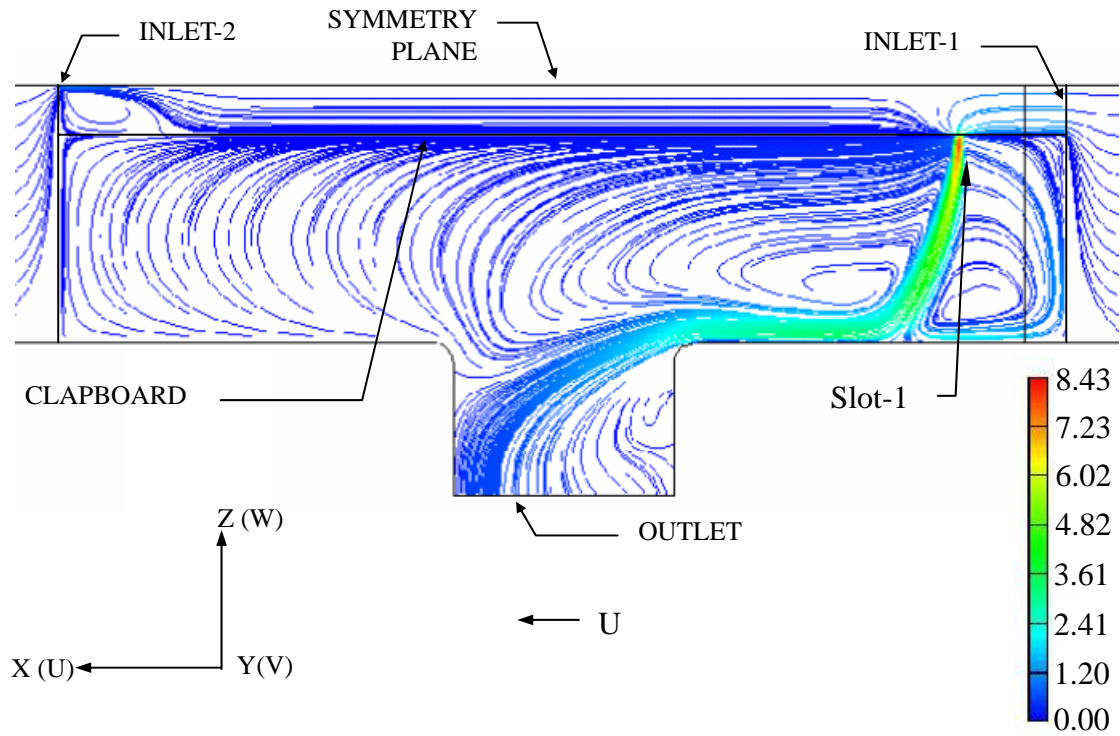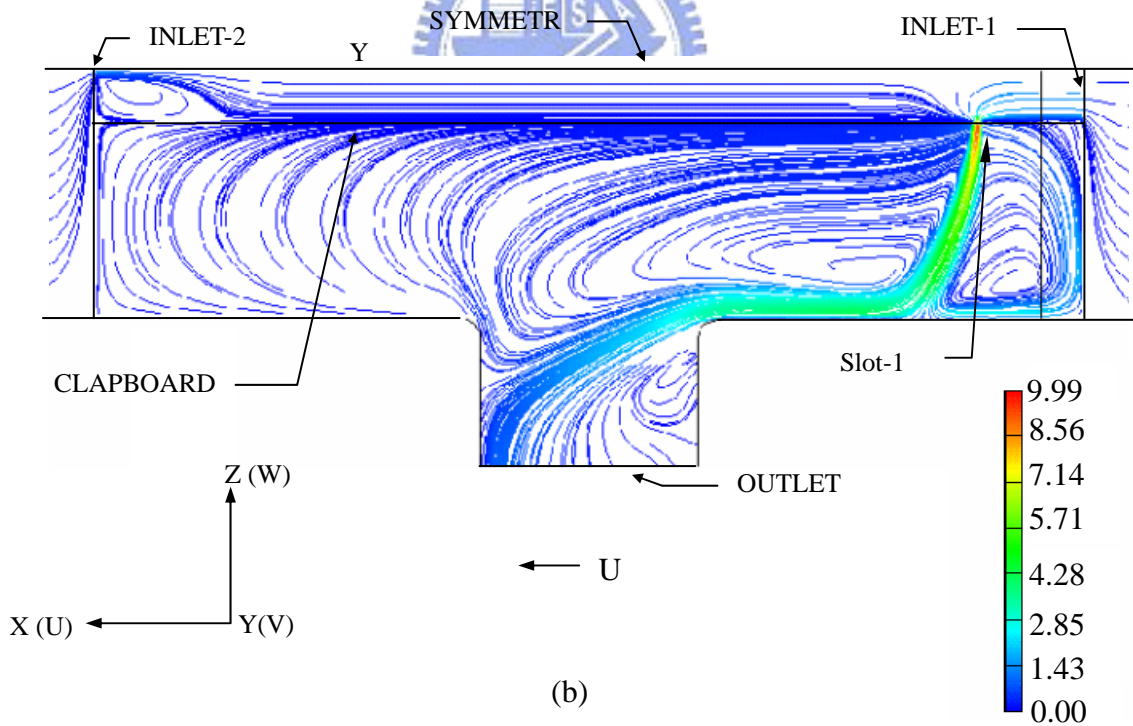
Fig. 3-11. A complete view of streamlines at the central plan (y = 2.5 mm) under (a) pressure drop 50 Pa and (b) pressure drop 70pa, between far-field pressure boundary and outlet pressure boundary.
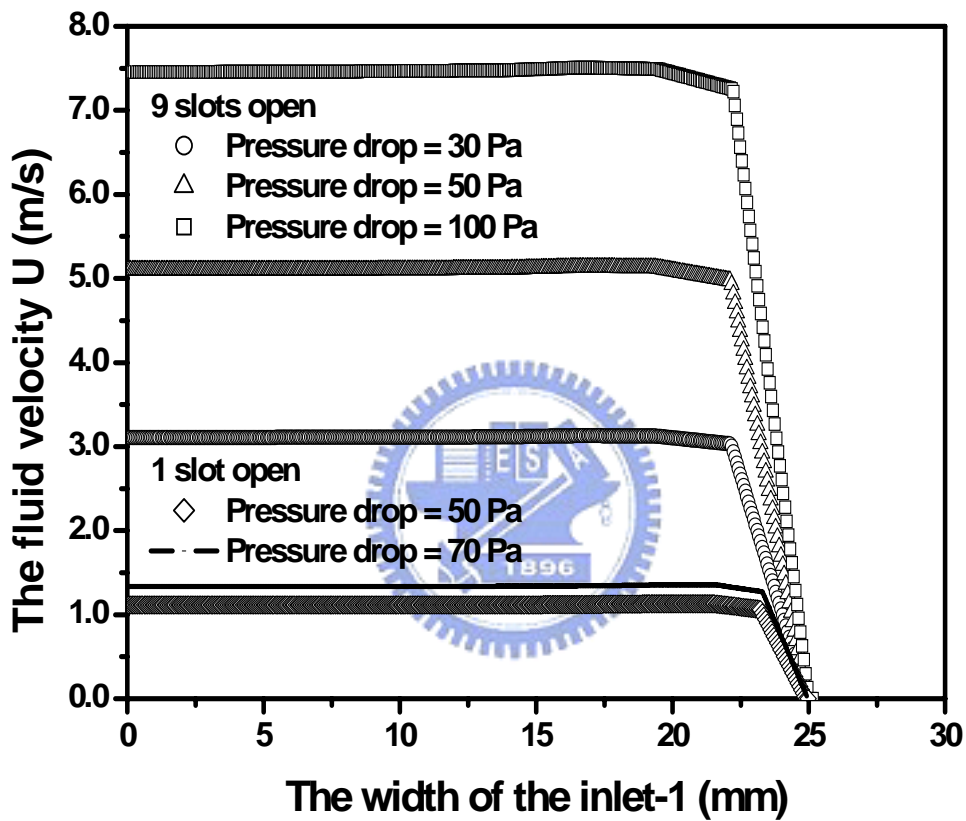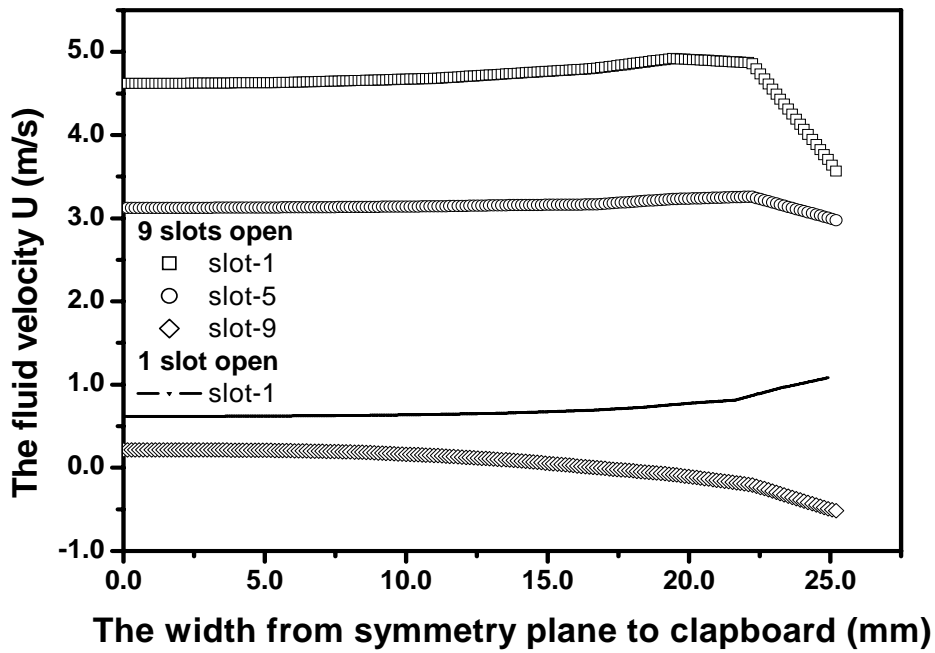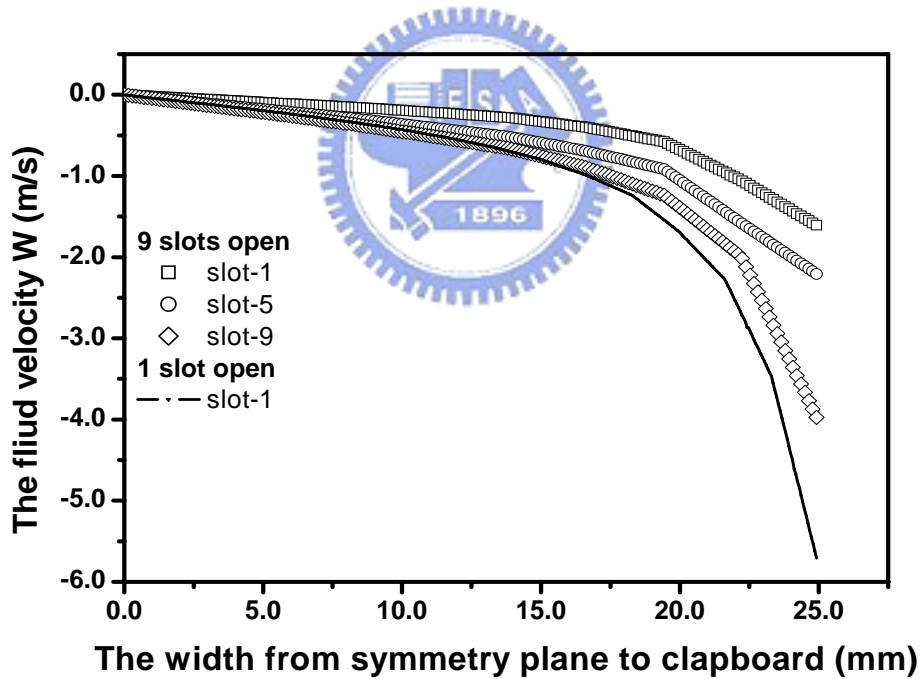
Fig. 3-12. Comparison of calculated U-velocity components from symmetry plane (width at 0 mm) to the clapboard (width at 25 mm) at the inlet-1, between the spreader with nine slots open and one slot open

(a)

(b)

Fig. 3-13. Comparison of calculated velocity components from symmetry plane (width at 0 mm) to the clapboard (width at 25 mm) in front of slots under the pressure drop = 50 Pa, between the spreader with nine slots open and one slot open (a) velocity U and (b) velocity W.

Fig. 3-14. Photographs of carbon fibers spread experiment under $V_F = 6$ m/min and Q = 110 L/min: (a) fibers spread and fluffy, (b) more fibers moved to lateral side, and (c) final state.
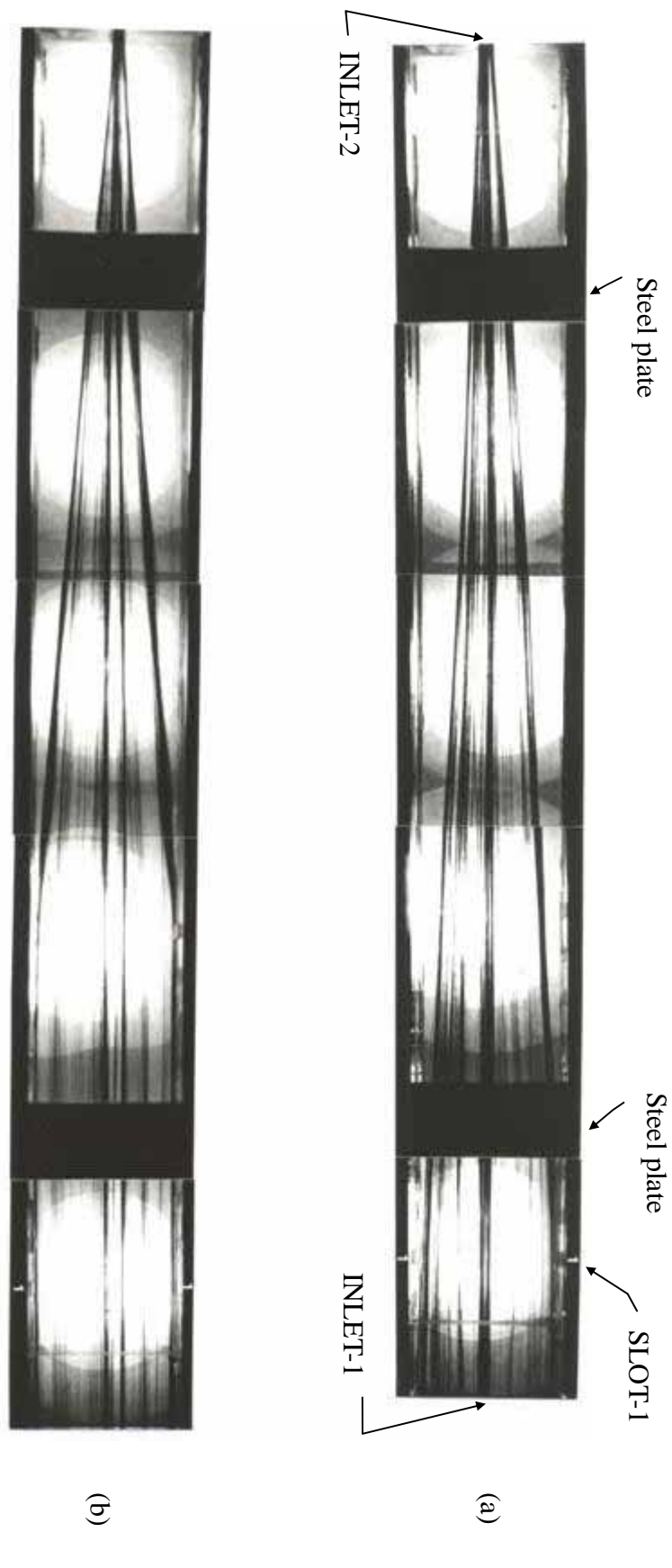
Fig. 3-15. Photographs of fibers spread experiment under $V_F = 5$ m/min and (a) Q = 105 L/min and (b) Q = 125 L/min.
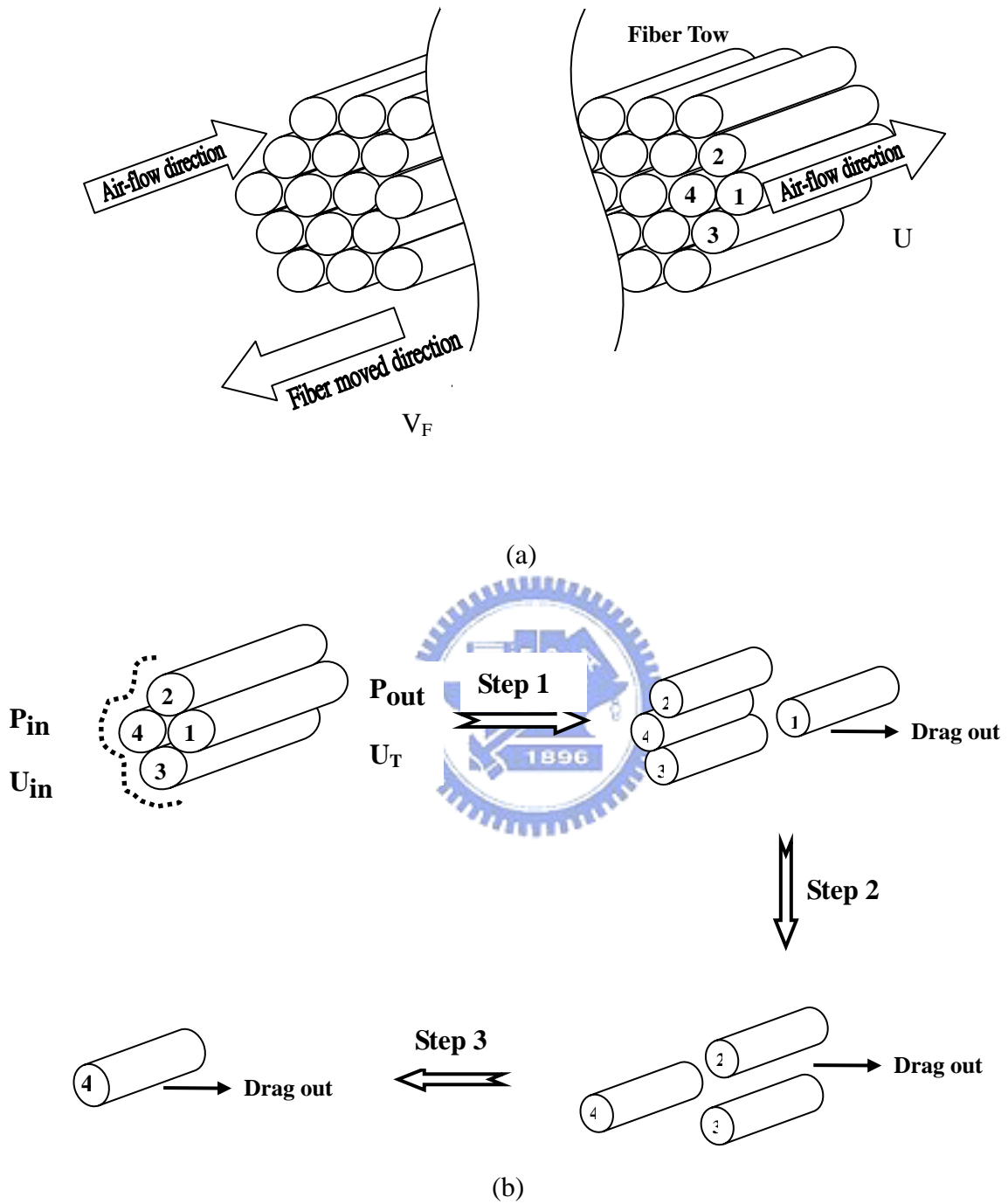
123

(a)

(b)

Fig. 3-16. Schematic of the mechanism for expressing the procedures during separation in a carbon fiber tow (a) fiber tow located between slot-1 and inlet-1, (b) a detailed illustration in fiber spreading steps.